CAAP Quarterly Report

[06/27/2024]

Project Name: "All-in-One Multifunctional Cured-In-Place Structural Liner for Rehabilitating of Aging Cast Iron Pipelines"

Contract Number: 693JK32250009CAAP

Prime University: North Dakota State University

Prepared By: [Ying Huang, ying.huang@ndsu.edu, 701-231-7651]

Reporting Period: [03/28/2024 – 06/27/2024]

Project Activities for Reporting Period:

In the 6th quarterly report, Tasks 2.1, 2.2, 3.1, 3.3, 3.4, 4.1, 4.2, and 5.1 were carried out as proposed. In this quarter (Quarter 7), the research team has made consistent progress on the selected tasks. Summaries of the key activities completed during the 7th reporting period are provided below.

Task 2.1 Preparation of Vitrimer Epoxy Resins, Characterization, and Optimization of the Processing and Curing Conditions (85%): In the last report, an excellent UV curing rate was found for the developed self-healing resin (formulation of DFMA: RDMA). The research team (Dr. Long Jiang and Austin Knight, Ph. D. student from NDSU) further investigated the effects of adding nanoparticles in the developed polymer. Additionally, a new photoinitiator was applied to further improve the curing rate. The key findings are presented below:

(1) Nanoparticle Reinforced Resin UV-Curing Rate Through Liner: Figure 1 shows the curing rate over time for samples of neat UV-curable self-healing resin and resin containing nanodiamonds (ND). The samples were cured both 1) on their own and 2) with a liner covering on top.

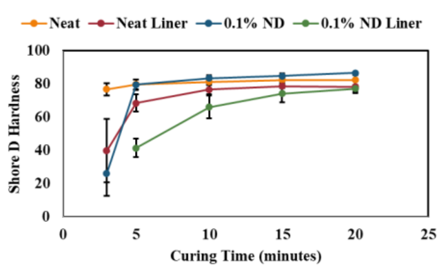

Figure 1. The Shore D Hardness of neat and ND resin through a CIP liner.

The hardness increased over the course of 20 minutes of curing. The presence of the liner and nanoparticles dispersed in the resin both increased the time required to cure the resin fully due to UV-absorption.

(2) Increasing Curing Rate with New Photoinitiator: To increase the curing rate and depth of nanoparticle-containing resins, the photoinitiator (PI) was changed to a more reactive PI that decomposes at a higher UV-light wavelength. The new PI cured the neat resin in less than 10 seconds, achieving a higher hardness than the old PI did after 15 minutes. The new PI also cured the 0.5% ND resin in 30 seconds, whereas the old PI took 15 minutes to solidify and could only cure to a depth of 1.5-2 mm (Figure 2).

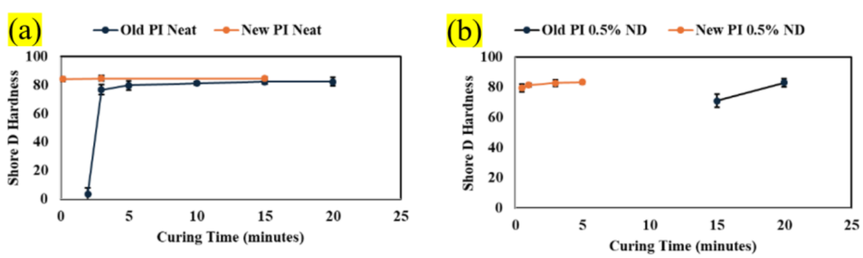

Figure 2. The curing rate of (left) the neat and (right) the 0.5% ND formulations.

(3) Curing Depth with New Photoinitiator: The curing depth of the resin is a crucial characteristic that determines the maximum thickness of adhesive that can be cured in the CIP system. Resin samples with different nanoparticles and concentrations were pipetted into an opaque mold and cured. The mold was 4 mm deep, representing the maximum achievable curing depth (Figure 3).

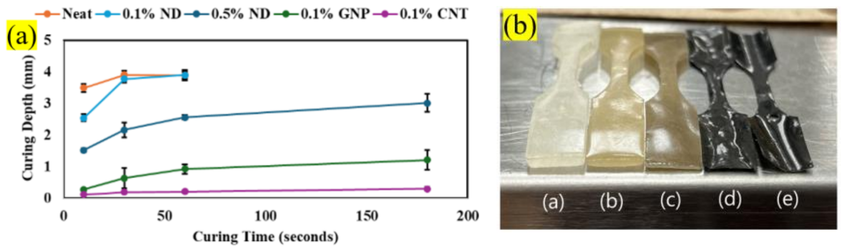

Figure 3. The curing thickness of various formulations, and the specimen of neat, 0.1% ND, 0.5% ND, 0.1% GNP, and 0.1% CNT formulations after being UV-cured for 10 seconds.

Task 2.2 Investigating Self-healing and Mechanical Properties of Vitrimer Epoxy Resins (60%): The research team (Dr. L. Jiang, Dr. Y. Huang, and Austin Knight, Ph. D. student from NDSU) continued investigating the self-healing polymer with various formulations to lower the required temperature for the resin to heal, and the mechanical properties of the new formulations are presented below:

(1) Mechanical Properties with Varied Homopolymers: Four monomers were UV-cured into homopolymers and tested to get a baseline of their mechanical properties, including difunctional methacrylate (DFMA), difunctional acrylate (DFA), reactive diluent methacrylate (RDMA), and reactive diluent acrylate (RDA). RDMA was very brittle compared to RDA, and both DFMA and DFA had high viscosities at room temperature. The better properties of DFA over DFMA is thought as more reactive acrylate groups leading to a higher crosslinked polymer (Figure 4).

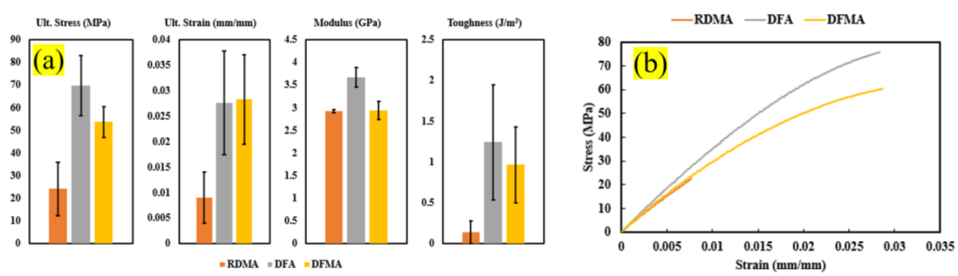

Figure 4. (a) The tensile properties of DFMA, DFA, and RDMA. (b) the representative tensile curves.

(2) Copolymer Mechanical Properties: The two difunctional monomers (DF) and two reactive diluents (RD) were mixed at a 1:1 acrylate/methacrylate functional group ratio to create four formulations. The formulation used in the previous report is labeled as DFMA: RDMA. The formulations containing RDA exhibited a higher ultimate strain, lower modulus, and higher toughness compared to those with RDMA. A similar trend was observed when comparing DFMA and DFA. Surprisingly, the ultimate strengths of all formulations were very similar to each other (Figure 5).

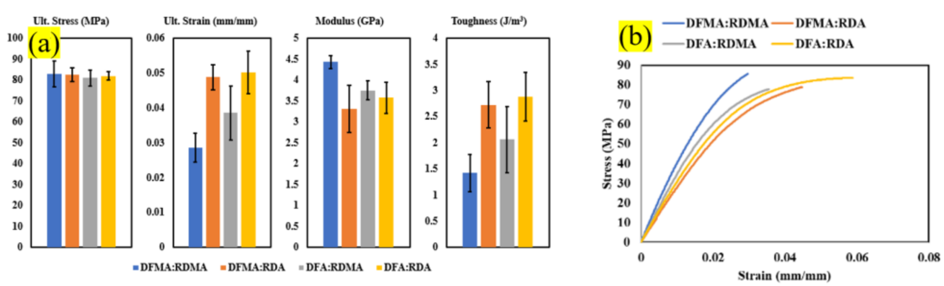

Figure 5. (a) The tensile properties of DFMA: RDMA, DFMA: RDA, DFA: RDMA, and DFA: RDA. (b) The representative tensile curves.

Task 3.1 High Mechanical Performance (80%): During this reporting period, the research team (Dr. Ying Huang, Dr. Xingyu Wang, and Muhammad Imran Khan, Master student from NDSU) conducted an experimental study on nanoparticle reinforcement on the developed self-healing polymer (DFMA: RDMA). The key findings are provided below:

(1) Mechanical Properties Improvement of Nanodiamond in Self-healing Polymer: Based on previous results, the 0.5% ND demonstrated excellent mechanical properties in commercially available epoxy polymers and showed no significant impact on the UV-curing rate of the developed self-healing polymer. The spherical geometry of ND plays a vital role in enhancing the composite's microstructure and minimizing UV light blockage during the curing process. Therefore, 0.5% ND reinforcement was selected for further evaluation. Figure 6 shows that 0.5% ND increased the flexural properties of the self-healing polymer.

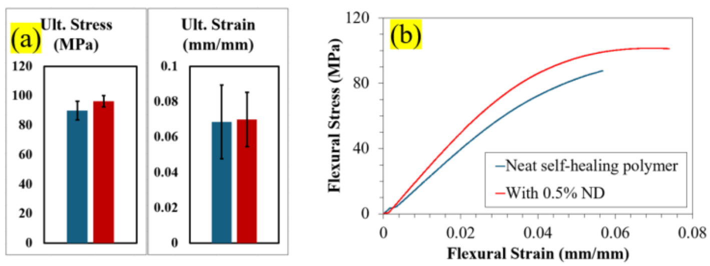

Figure 6. (a) The flexural properties of self-healing polymer with 0.5% of ND and (b) the representative stress vs. strain curves.

Task 3.3. Reducing the Permeability and Investigating the Interfacial Bonding Chemical Analysis (55%): Previously, the research team (Dr. Liangliang Huang, Qiuhao Chang, Ph. D. student from University of Oklahoma) investigated the hydrogen diffusion process using developed nanopore models and initiated the development of vitrimer models. In this reporting period, we investigated hydrogen adsorption in the non-reactive vitrimer model, and also examined the impact of hydrogen sulfide (H_2S) on gas-water interfacial tension and permeability:

(1) Hydrogen Adsorption in the Developed Non-reactive Vitrimer Model: Adsorption calculation of hydrogen in the non-reactive vitrimer model was performed at 300 K and 1 atm. To explore the maximum loading of hydrogen in the non-reactive vitrimer model, we calculated 10^5 MC runs with the Metropolis method to equilibrate the system, followed by 10^8 production steps, and the results were presented in Figure 7.

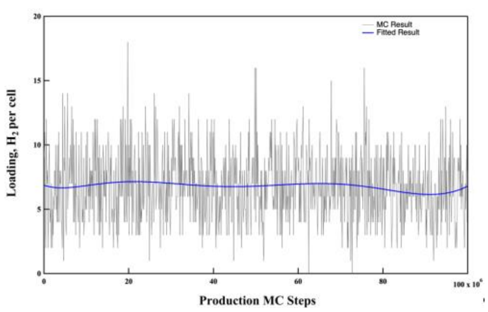

Figure 7. Hydrogen loading in the non-reactive vitrimer model at 300 K and 1 atm.

Three movements, namely, exchange, rotate, and translate, were randomly sampled in the ratio of 20:1:20. The average loading of hydrogen was reported to be 6.833 H_2 molecule/cell, with the isosteric heats of 1.063 kcal/mol. It is worth noting that the vitrimer has a chemical formula of C7992H8288N296O1184S296. Therefore, the loading of 6.833 H_2 molecule/cell suggests that there is negligible hydrogen adsorption in the vitrimer.

(2) Analysis of Hydrogen Sulfide's (H_2S) Impact on Gas-water Interfacial tension: We leverage molecular dynamics simulations to elucidate the dynamics of interfacial tension between residual water and gas mixtures comprising hydrogen (H_2), methane (CH_4), and H_2S within the porous media. The findings significantly advance our understanding of in-pore storage and transport mechanisms by demonstrating that even a minimal concentration of H_2S leads to a considerable reduction in interfacial tension (IFT), a factor critical for optimizing pipeline hydrogen transport operations. As shown in Figure 8, interfacial properties such as adsorption, absorption, and orientation affect the gas-water interfacial properties. The density profiles we observed in Figure 8 show notable variations among the different gases at the interface. H_2 exhibited a pronounced

reduction in density near the interface, suggesting the minimal presence of H_2 molecules within this region. In contrast, the density of CH_4 peaked at the interface, indicative of CH_4 adsorption at the interface, highlighting the affinity of CH_4 molecules for this boundary and echoing the observations of several prior studies. The H_2S profile was particularly distinct, revealing a significant concentration of H_2S molecules within the interface region, which can be interpreted as a result of H_2S absorption into the water phase.

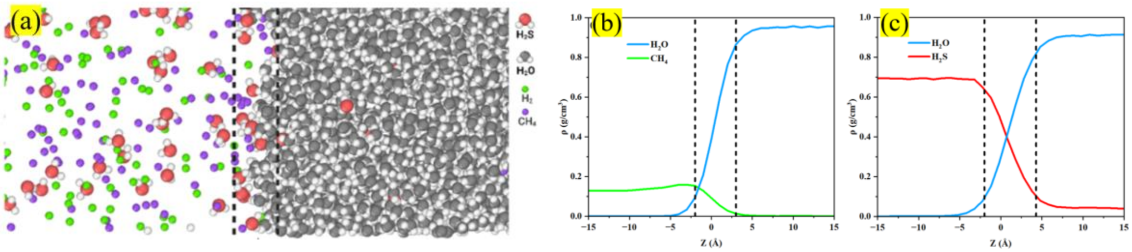

Figure 8. (a) The schematic illustration of the gas-water interface, Density profiles at 343 K and 14.5 MPa: (b) CH_4-H_2O; (c) H_2S-H_2O.

Task 3.4 Finite Element Numerical Analysis to Guide the Design of the Developed High-performance Healable CIPP Structural Liner (70%): During this reporting period, the research team (Dr. Chengcheng Tao, Junyi Duan, Ph.D. student from Purdue University) have conducted finite element analysis (FEA) for pipelines with CIPP liners. Continuing from the previous report, the following presents the effects of corrosion holes in the liner-protected elbow pipe and results are as summarized below:

(1) The Effect of Corrosion Hole Size in Liner Protected Elbow Pipes: To assess the impact of corrosion hole dimensions on the integrity of an elbow pipe system, a 25 mm radius corrosion hole was created at the midpoint of the inner wall. The effects on the corroded elbow pipe system are presented in Figure 9.

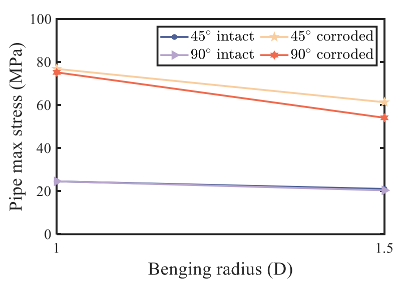

Figure 9. The normalized stress of CIPP liner system with respect of corrosion hole size. (ad = adhesive layer)

Results indicated the effect of elbow angle becomes noticeable when the pipe is corroded. A 45-degree corroded elbow pipe exhibits higher axial tensile stress compared to a 90-degree one, and the difference increases with the bending radius.

(2) The Effect of Corrosion Hole Location in Liner Protected Elbow Pipes: Five locations were selected for corrosion hole: the midpoints of inner and outer walls (Figure 10), the midpoints at the top and bottom of the walls, and the top connection point between straight and elbow pipes. The results suggest that the pipe with a corrosion hole at the midpoint of the inner wall exhibits the highest tensile stress compared to others. Following this, the pipe with holes at the wall's top connection point, mid-top, and mid-bottom show similar stress performances. The lowest stress concentration is observed in the pipe, with corrosion at the outer wall.

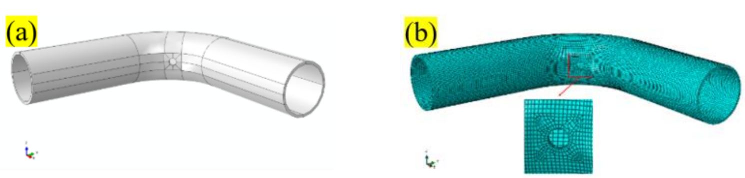

Figure 10. The geometry (a) and mesh (b) of the elbow pipe with corrosion hole model.

(3) The Effect of Adhesive Layer Thickness in Liner Protected Elbow Pipe with a Corrosion Hole: To investigate the effect of adhesive layer thickness on an elbow pipe system, a 25-mm radius corrosion hole at the midpoint of the inner wall was selected as the imperfection. Various adhesive

layer thicknesses, ranging from 0.25 to 1 mm, were tested. Figure 11 illustrates the maximum stress experienced by the pipe, liner, and adhesive layer as a function of adhesive layer thickness. The findings suggest that an adhesive layer thickness of 0.5 mm is most effective for this scenario.

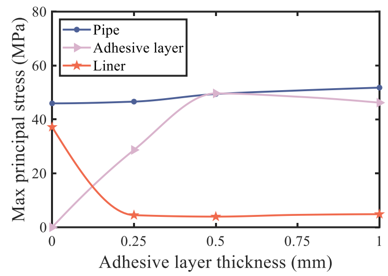

Figure 11. The mechanical performance of corroded elbow pipe system with 25-mm-radius hole with varied adhesive layer thickness.

The stress of the liner decreases significantly with a thicker adhesive layer up to 0.25 mm, and tends to plateau with continuous increment. Meanwhile, the stress within the adhesive layer continues to rise until it reaches 0.5 mm in thickness, and then slightly decreases when it exceeds 0.5 mm.

Task 4.1 Development of Embedded Distributed Fiber Optic Sensors for Self-sensing Structural Liner (65%), and **Task 4.2** Investigating the Load Transfer between Layers of the CIPP Liner and the Cast-iron Substrate (50%): During this reporting period, the research team (Dr. Ying Huang and Dr. Xingyu Wang) continued the study on smart-liner system, focusing on converting strain signals into deflection measurements during buckling deformation of the liner. Additionally, they developed 3-D digital twin models of the specimen to depict the progression of shape changes throughout the experiment. The findings are summarized below:

(1) Strain Validation with FEA simulations: The strain distribution obtained from distributed fiber optic sensors and FEA are compared in Figure 12. The strain patterns and magnitudes recorded by the sensors are highly matched to the prediction by FEA, underscoring its efficacy in monitoring surface strain changes, thereby affirming the smart-liner's utility.

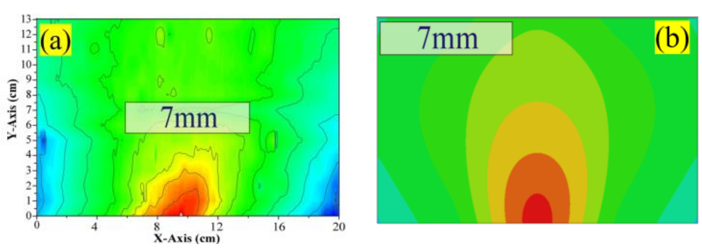

Figure 12. Strain distribution on the smart-liner protected specimen when displacement reached 7 mm, derived from (a) sensor data and (b) FEA model predictions.

(2) Investigation on Strain-deformation Models and Creation of Digital Twin Models: The deformation of the smart-liner protected specimen was reconstructed using the developed analysis method (Figure 13), and the 3-D digital-twin models of the specimen were developed (Figure 14).

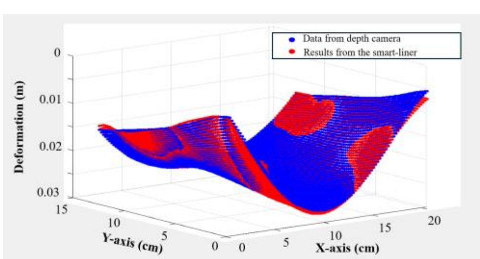

Figure 13. Deformation of the liner protected specimen obtained from shape reconstruction (red dots) and computer vision (blue dots).

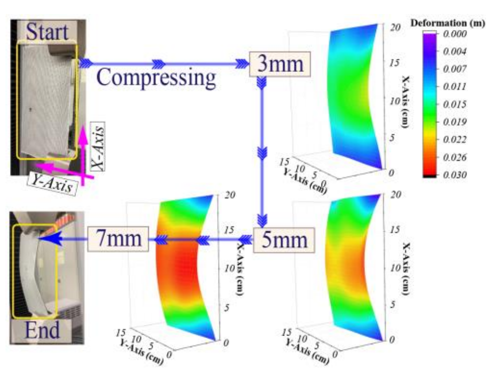

Figure 14. 3-D digital twin-based virtual models for specimen under buckling deformation.

The reconstructed shape was then processed with the point cloud data generated by the computer vision system (Figure 13). There is a commendable alignment between the reconstructed shape and the measured deformation, indicating the accuracy of the reconstruction method. After that, the deformation progress of the specimen was utilized to generate digital twin-based models (Figure 14). The inclusion of displacement is crucial, as it progressively increases throughout the duration of the experiment, providing a direct correlation between the physical deformation of the smart-liner and its virtual representation. This sequence of virtual models underscores the smart-liner system's advanced ability to track and visualize the evolution of a physical asset in real-time.

Task 5.1 Development of CIPP Liner Risk Index for the Pipeline Integrity Management Enhanced by AI Algorithms (50%): During this reporting period, the research team (Dr. Chengcheng Tao, Huaixiao Yan, Ph.D. student from Purdue University) have conducted the risk assessment using dataset generated from finite element analysis for pipeline integrity management, with the results outlined below:

(1) Bonding Risk Map at the Corrosion Hole: In this task, we created bonding risk maps at the corrosion hole area in the pipe-liner system by training the displacement and stress dataset generated from previous finite element analysis. Five machine learning algorithms are applied to train (80%) and test (20%) the dataset. Table 1 shows the accuracy of the five algorithms. Figure 15(a) shows the effect of various parameters, such as adhesive layer thickness, hole size, and internal pressure on stress and displacement. Internal pressure has a greater impact on the stress and displacement at the corrosion hole area. As shown in Figure 15(b), the random forest algorithm provides an accurate prediction on the displacement. Figure 15(c) and (d) demonstrate the risk map predicted by machine learning algorithms using the displacement and stress data on the bonding surface between the pipe and adhesive layer.

Table 1. Accuracy of different algorithms

Algorithms	Prediction types	R^2	MSE	MAE
Random Forest	Stress	0.83	16.04	1.88
	Displacement	0.88	4.90	0.88
XGBoost	Stress	0.97	2.79	0.74
	Displacement	0.99	0.60	0.40
LightGBM	Stress	0.71	26.80	2.99
	Displacement	0.69	14.67	2.09
Support Vector Machine	Stress	0.57	28.60	2.58
	Displacement	0.64	14.62	1.67
Gaussian Process	Stress	0.99	1.27	0.48

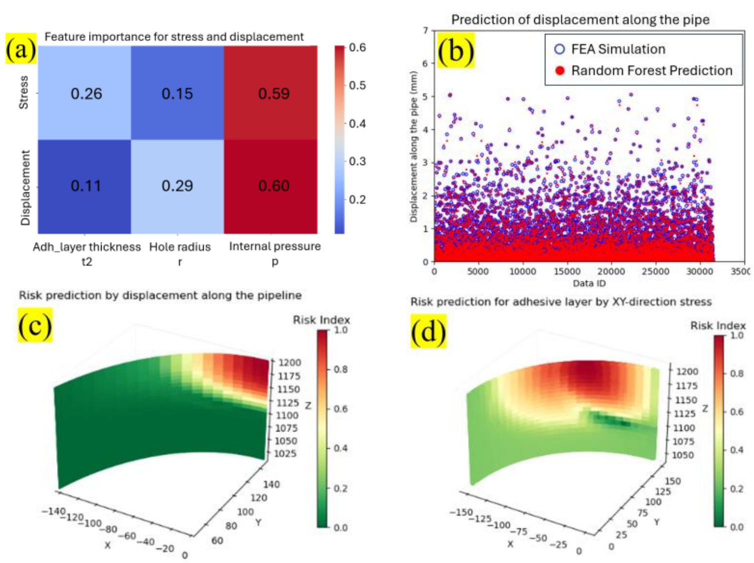

Figure 15. (a) Sensitivity analysis; (b) comparison between machine learning prediction data and FEA data. Risk map at corrosion hole area using (c) relative displacement data and (d) stress data on the bonding surface between the pipe and adhesive layer.

For the displacement risk map, we normalize displacement data to 0 (green) to 1 (red) to represent low risk and high bonding risk in the damaged area. The green area indicates the safe area, the yellow area indicates the critical area, and the red area indicates the high-risk area.

Project Financial Activities Incurred during the Reporting Period:

The cost breakdown during the reporting period in each category according to the budget proposal is shown in Table 2.

Table 2. Cost breakdown

Category	Amount spent during Q7
Personnel	
Faculty	$0.00
Postdoc	$15,408.66
Students (RA and UR)	$16,191.77
Benefits	$8,218.35
Operating Expenses	
Travel	$0.00
Materials and Supplies	$1,975.49
Recharge Center Fee	$2,733.00
Consultant Fee	$1,639.00
Subcontracts	$8,558.19
Indirect Costs	$20,774.89

Project Activities with Cost Share Partners:

The Match fund from NDSU for this project is coming from the tuition of the associated graduate students during their work on this project. During the reporting period (Q7), Zahoor Hussain (100%), Muhammad Imran Khan (100%), Austin Knight (100%), and Tofatun Jannet (100%) were hired on the project. The tuition for the four students during Q7 was estimated to be $5,564 at a rate of $463.73 per credit.

Project Activities with External Partners:

During this reporting period, George Ragula, our industry consultant, attended all the bi-weekly meetings with the research team.

Potential Project Risks:

No potential risks were noticed during this reporting period.

Future Project Work:

The research team will continue working on Tasks 2.1, 2.2, 3.1, 3.2, 3.3, 3.4, 4.1, 4.2 and 5.1.

Potential Impacts on Pipeline Safety:

The newly developed self-healing epoxy (DFMA: RDMA) demonstrates an excellent UV curing rate and compatibility with both liners and nanoparticles. In the meantime, the nanodiamond showed good improvement on mechanical properties in the developed self-healing epoxy polymer; combining the benefits of self-healing polymers and nanoparticle reinforcement to create a high-performance, repairable liner. Molecular dynamics simulations were developed to analyze the dynamics of interfacial tension between residual water and gas. Finite element analysis (FEA) has provided insights into the effects of corrosion holes on the maximum allowable stress in both straight and elbow liner systems. Parallel to these findings, we have started developing risk analysis models to predict the performance of the liner system. The innovative data analysis method enables the smart-liner system to convert strain signals into deflection measurements and generate 3-D digital twin models when the liner undergoes deformation, offering a promising approach for real-time monitoring and optimization of pipelines.